CrossMark

A Feasibility Study of the Pore Topology Method (PTM), A Medial Surface-Based Approach to Multi-phase Flow Simulation in Porous Media

M. Sadegh Riasi[1] · **Nikhil Kumar Palakurthi**[2] ·
Carlo Montemagno[3] · **Lilit Yeghiazarian**[1]

Abstract Computationally efficient microscale models designed to simulate multi-phase flow and characterize low-porosity media are challenged in thin, highly porous materials, primarily due to large, irregular pore spaces and inability to satisfy representative elementary volume requirements. In this article, we describe the pore topology method (PTM) and explore its capabilities to characterize a set of isotropic fibrous materials and to simulate multi-phase flow. PTM is a fast, algorithmically simple method that reduces the complexity of the 3-D void space geometry to its topologically consistent medial surface and uses it as a solution domain for single- and multi-phase flow simulations. Our results in permeability calculations, pore size distribution, and quasi-static drainage and imbibition simulations are in very good agreement with other numerical methods and analytical solutions. We expect that incorporating detailed spatial information about the porous media structure into the medial surface will enable a more accurate representation of the void space structure and of physical phenomena involved in multi-phase flow, thus expanding the applicability of PTM to a broader range of porous media, including non-fibrous materials.

1 Introduction

Thin, highly porous materials are ubiquitous in nature and widely employed in many products and devices. Examples range from living tissues, filters, membranes, and absorbent materials

---

✉ Lilit Yeghiazarian
  yeghialt@ucmail.uc.edu

[1] Department of Biomedical, Chemical and Environmental Engineering, University of Cincinnati, Cincinnati, OH, USA

[2] Department of Mechanical and Materials Engineering, University of Cincinnati, Cincinnati, OH, USA

[3] Department of Chemical and Materials Engineering, University of Alberta, Edmonton, AB, Canada

to fuel cells and microfluidic devices, driving the need to better understand the structure and processes in these materials. Their distinct properties, however, present new challenges in experimental and numerical characterization.

Thin, highly porous materials are characterized by thickness on the order of pore dimension (Prat and Agaësse 2015) and by porosity of larger than 60 % (Gervais et al. 2012; Gostick 2013; Si et al. 2015). Therefore, representative elementary volume (REV) requirements cannot be satisfied, and macroscale theories of transport do not hold (Qin and Hassanizadeh 2014). Furthermore, large, irregular pore spaces preclude easy characterization of the pore space geometry. Microscale models of flow in thin, highly porous media are promising; however, their implementation is not trivial. Some of the challenges include computational cost and convergence in direct numerical simulation methods (DNS) (e.g., Ahrenholz et al. 2008; Palakurthi 2014; Vennat et al. 2014), while computationally fast techniques (e.g., Bazylak et al. 2008; Ghassemzadeh et al. 2001; Ghassemzadeh and Sahimi 2004; Gostick et al. 2007; Hinebaugh and Bazylak 2010; Koido et al. 2008; Lee et al. 2010, 2009; Markicevic et al. 2007; Pan et al. 1995; Wu et al. 2012) need to overcome difficulties in capturing the pore size distribution (Gostick et al. 2007) and computing respective entry capillary pressure (Joekar-Niasar et al. 2010; Lindquist 2006; Prodanović and Bryant 2006), as well as in detecting the correct location of fluid interfaces for a range of contact angles (Frette and Helland 2010; Schulz et al. 2015).

To address these challenges, we have conducted a feasibility study on using medial surfaces as both the representative geometry and the solution domain for multi-phase flow simulations. We refer to this approach as the pore topology method (PTM). Medial surfaces are widely used in biomedical imaging with applications in surface reconstruction and dimension reduction of complex objects (Styner et al. 2004; Sun et al. 2010; Vera et al. 2012b). In porous media research, they have been suggested as a powerful tool to gain insight into complicated geometries (Prodanovic and Bryant 2009) and as the correct approach to pore space representation, likely to improve on pore network modeling and on morphological methods in capturing sheet-like pores (Wildenschild and Sheppard 2013). In this direction, Jiang et al. (2012) extended their skeletonization-based pore network extraction algorithm (Jiang et al. 2007) and developed a modified version of a medial surface to locate and quantify fractures. In their work, the medial surface was used as an intermediate step in generating a pore network model. The medial surface was converted to virtual nodes and bonds and then added to a traditional pore network model, hoping to better represent fractures in a pore network model of a fractured porous media. Later, Corbett et al. (2015) used this approach to characterize microbial carbonates. To authors' knowledge, a direct use of medial surface has not been reported in porous media literature, neither as a representative geometry nor as the solution domain.

Here, we expand on our recent work (Riasi et al. 2013) and apply PTM to a series of isotropic fibrous materials with different porosities (25–95 %). We have extracted the medial surface of the void space, derived the pore size distribution, computed the absolute permeability, and simulated quasi-static drainage and imbibition using the medial surface as the solution domain. Comparison of results with lattice Boltzmann, full morphology, volume of fluid and finite volume methods, as well as exact solutions, showed a very good fit.

The outline of this article is as follows: We present the definition and properties of a medial surface, followed by a brief description of the extraction algorithm, in Sect. 2.1. Details of the algorithm are presented in "Appendix 1." We describe absolute permeability calculation in Sect. 2.2 and quasi-static drainage and imbibition simulations in Sect. 2.3. We present and discuss our results in Sects. 3 and 4 and conclude the paper with Sect. 5.

2 Methods

2.1 Medial Surface

2.1.1 Definition and Properties

Medial surfaces of 3-D objects were first proposed by Blum (1967) as shape descriptors and defined as "the loci of center of maximal spheres bi-tangent to the surface boundary points of the shape." Along the same lines, Price et al. (1995) described them as "the locus of the center of an inscribed sphere of maximal diameter as it rolls around the interior of the object." For differences between medial axis and medial surface, please refer to classic works of Lee et al. (1994) and Lindquist and Venkatarangan (1999).

An ideal medial surface of an object satisfies three conditions (Vera et al. 2012a): (i) homotopy: preserving the topology of the original object, (ii) thinness and connectivity: generating a fully connected, voxel-wide medial surface; and (iii) medialness: generating a medial surface that is as close as possible to the center of the object in all directions. These properties collectively stipulate that the medial surface of an object offers its compact representation, while retaining sufficient local information to reconstruct the object fully and with high accuracy. If the object in question is the void space of a porous medium, then homotopy and medialness of its medial surface would ensure that all corners and curvatures are captured, while thinness and connectivity would ensure that pore connectivity in void space is preserved.

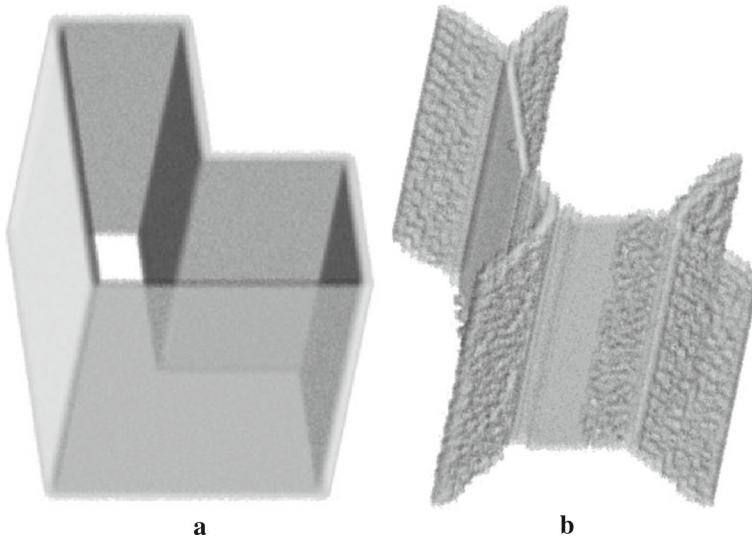#### 2.1.2 Medial Surface Extraction Algorithm

Several approaches have been proposed to extract a voxel-wide medial surface of a 3-D object, mostly based on iterative thinning of an energy map; one example is distance maps (Bouix et al. 2005; Lee et al. 1994; Pudney 1998). We used Multilocal Level-Set Extrinsic Curvature based on the Structure Tensor (MLSEC-ST) developed by Lopez et al. (2000) as described in Vera et al. (2012a). MLSEC-ST is a non-iterative analytical approach that is shown to be less sensitive to noise, have higher reconstructive power compared to other available algorithms, and produce surfaces that closely satisfy the conditions of an ideal medial surface (Vera et al. 2012a). We have modified the last step of the algorithm, medial surface thinning, to ensure full connectivity in the final medial surface. A detailed description of the modified MLSEC-ST algorithm applied to a simple prism (Fig. 1) is given in "Appendix 1."

2.2 Absolute Permeability Calculation

To compute absolute transverse permeability, we assumed a steady-state, laminar, single-phase flow through the void space of porous medium. To compute the fluid pressure (P) distribution inside the void space, we solved the following equation on the medial surface using the finite volume method:

$$\nabla \cdot (K_{\text{local}} \nabla P) = 0 \tag{1}$$

where K_{local} is the local hydraulic conductivity at each voxel of the medial surface. To determine K_{local}, we assumed that single-phase flow at each voxel was influenced mainly by its nearest solid walls and therefore used the Poiseuille equation for flow between parallel plates. To test the validity of the planar flow assumption, we computed hydraulic conductivities for a set of prisms with polygonal cross sections and compared the result with exact solutions

Fig. 1 A 3-D model of a constant cross-sectional prism (**a**) and its medial surface extracted using the modified MLSEC-ST method (**b**)

("Appendix 2"). Note that for each voxel, all 26 neighboring voxels should be included in discretizing Eq. (1) (see detailed discretization in "Appendix 3").

Solving the Navier–Stokes equation for single-phase, steady-state, fully developed, laminar, pressure-driven flow between two parallel plates, we obtained the following expression for the local hydraulic conductivity at each voxel:

$$K_{\text{local}} = \frac{2}{3}(br^3/\mu) \tag{2}$$

where μ is the fluid viscosity, b is the voxel size, and r is the distance between the medial surface voxel and the closest solid boundary. The boundary conditions for Eq. (2) are similar to Fig. 2, but with reservoirs replaced with two non-equal wetting phase pressure conditions.

From the pressure field inside the void space, the flow rate can be calculated at the boundary of the porous medium:

$$Q = \sum_{\text{boundary voxels}} \left(-K_{\text{local}} \frac{\partial P}{\partial x}\right) \tag{3}$$

The absolute permeability k can then be calculated as

$$k = -\frac{Q\mu L}{A\Delta P} \tag{4}$$

where L is the length of porous medium, $A = w_1 \times w_2$ (Fig. 2) is cross-sectional area, and ΔP is the applied pressure difference across the medium.

2.3 Quasi-Static Drainage and Imbibition

The Young–Laplace equation states that capillary pressure difference across the interface of two static fluids P^c is a function of surface tension σ and the mean curvature of the interface H:
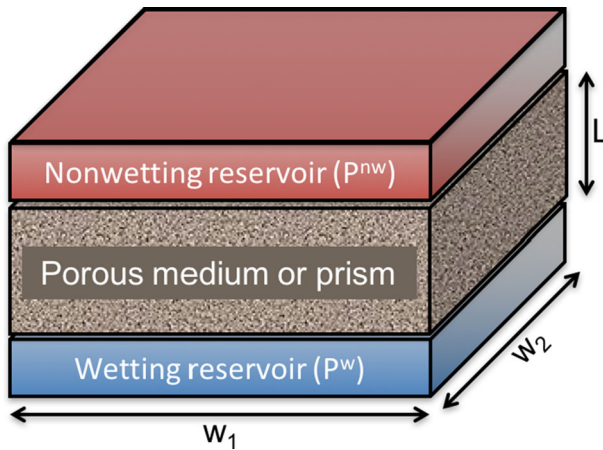
Fig. 2 Schematic of problem setup for quasi-static drainage and imbibition simulation and permeability calculation. Boundary conditions include non-wetting and wetting phase reservoirs at the *top* and the *bottom*, and no-flux conditions on sides

$$P^c = \sigma H = \sigma \left(\frac{1}{R_1} + \frac{1}{R_2} \right) \tag{5}$$

where R_1 and R_2 are the principal radii of curvature of the interface. For a finite, positive P^c, one can identify two opposite cases: (i) the spherical interface case, where $R_1 = R_2 = R$ and therefore $P^c = \frac{2\sigma}{R}$; (ii) the cylindrical interface case, where $R_1 = R$ and $R_2 = \infty$ and, therefore, $P^c = \frac{\sigma}{R}$. In reality, quasi-static interfaces span over this range (Vogel et al. 2005). Here, we use the average P^c of these two cases to approximate the entry capillary pressure at each voxel of the medial surface, yielding $P^c = \frac{1.5\sigma}{R}$. Assuming that the smallest radius of curvature R is related to contact angle θ through $R = \frac{r}{\cos(\theta)}$, where r is the distance between the medial surface voxel and the closest solid boundary, we obtain:

$$P^c = \frac{1.5\,\sigma\,\cos\,(\theta)}{r} \tag{6}$$

To test the validity of this assumption, we compared our drainage and imbibition results for prisms with triangular and rectangular cross sections, with the analytical results of Mason and Morrow (1991), with excellent agreement (not presented). To simulate quasi-static drainage and imbibition, medial surfaces of porous media samples were extracted from binary images as described in "Appendix 1," and an entry capillary pressure P^c_{entry} was assigned to each voxel on the medial surface using Eq. (6). For the setup shown in Fig. 2, the percolation of wetting phase (imbibition) or non-wetting phase (drainage) was simulated. For drainage, the wetting phase reservoir pressure was assumed to be zero and initially equal to the pressure of the non-wetting phase reservoir. To initiate drainage, the non-wetting phase pressure was increased until it exceeded the entry capillary pressure of voxels connected to non-wetting phase reservoir. At this pressure, the non-wetting phase can occupy voxels connected to the non-wetting phase reservoir, if $P^c_{\text{entry}} < (P^{\text{nw}} - P^w)$, where P^{nw} is the non-wetting phase reservoir pressure, and P^w is the wetting phase reservoir pressure. The drainage simulation proceeded by increasing the non-wetting phase pressure in increments, checking for the above-mentioned condition and propagating the non-wetting phase accordingly.

Imbibition simulation started from a large pressure difference ($P^{\text{nw}} - P^w$) corresponding to ∼0 % wetting phase saturation and continued by decreasing the non-wetting phase pressure

Table 1 Geometrical and physical parameters of fibrous samples used in this study

Property	Value	Unit
Dimension	$2 \times 2 \times 0.8$ (height)	mm
Porosity (φ)	0.25, 0.5, 0.7, 0.8, 0.9, 0.95	
Resolution	4	μm
Contact angle (θ)	55	Degree
Surface tension (σ)	0.0725	N/m
Viscosity of wetting phase (μ)	0.001	Pa s

in increments. At each pressure difference, the wetting phase can occupy voxels connected to the wetting reservoir, if $P_{\text{entry}}^{c} > (P^{\text{nw}} - P^{w})$. As evident from both drainage and imbibition algorithms, we assumed that no trapping occurred. We also ignored merging and splitting of interfaces.

For both drainage and imbibition, wetting phase saturation S^{w} was computed at each pressure difference:

$$S^{w} = \frac{\sum_{i} r_{i}}{\sum_{j} r_{j}} \tag{7}$$

where r is the minimum distance between each voxel of the medial surface and nearby solid clusters, $i = 1, \ldots, I$ where I is the number of medial surface voxels occupied by wetting phase, and $j = 1, \ldots, J$ where J is the total number of voxels on medial surface. Alternatively, one can compute the saturation values by reconstructing the saturated 3-D void space from the medial surface voxels that are occupied by wetting phase during drainage and imbibition, albeit at a much higher computational time. Our numerical investigations (not presented) showed that despite its simplicity, Eq. (7) produced negligible error compared to the 3-D volume reconstruction approach.

3 Results

We implemented PTM on six isotropic homogenous fibrous materials with different porosities. Fibrous is referred to materials made from natural or synthetic fibers. All structures were generated using the GeoDict software package. Table 1 below summarizes the geometrical and physical parameters of virtual porous media used in this study. Figure 3 shows a sample of fibrous material and its medial surface, and Fig. 4 shows cross sections of the virtual fibrous materials used in this study.

3.1 Pore Size Distribution

Pore size distributions were computed in GeoDict and PTM for all material samples, using porosimetric and geometric methods (Fig. 5). Porosimetric pore size distribution analysis is based on numerical modeling of the intrusion of a non-wetting fluid (mercury) into the void space of an air-occupied porous medium. GeoDict uses the full morphology (FM) method and PTM—the drainage algorithm described in Sect. 2.3.

The geometric pore size distribution in GeoDict is obtained by fitting spheres into the void space of the porous structure. In PTM, each voxel of the medial surface is associated with a
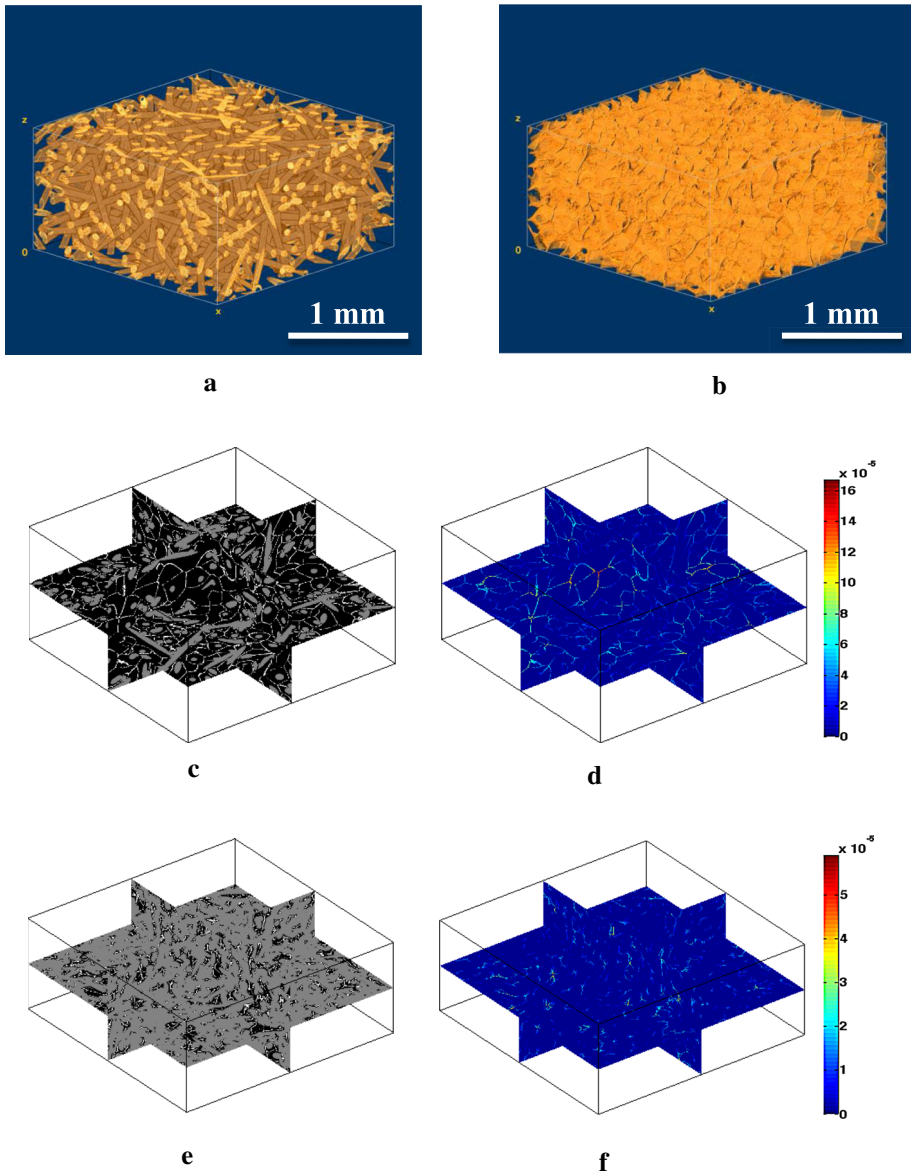
Fig. 3 **a** Virtual 80 % porous fibrous material generated with GeoDict; **b** medial surface; **c** sliced image showing fibers (*gray*), medial surface (*white*) and void space (*black*); **d** medial surface *colored* according to its distance map values; **e**, **f** sliced image for 25 % porous fibrous material colored similar to **c**, **d**

voxel-wide square prism with height of $2r$, where r is the minimum distance between each voxel and nearby solid clusters. Each prism represents a pore. The volume fraction is then calculated similarly to Eq. (7).

Figure 5 shows a rather critical problem associated with current pore-based methodologies such as pore network modeling and full morphology: the definition of pore. Although characterizing the pores through sphere fitting is an appropriate method for low-porosity,
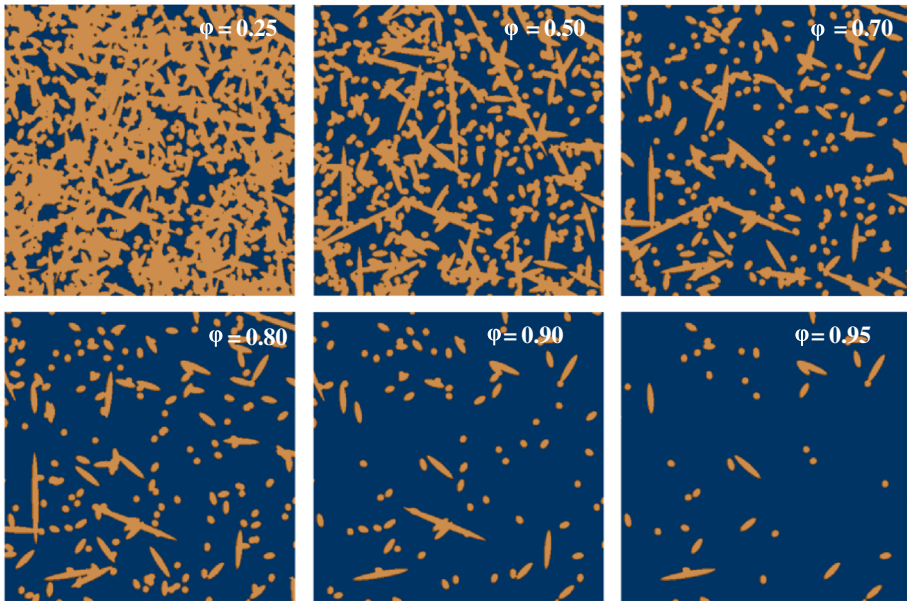
Fig. 4 2-D cross sections of the virtual porous media used in this study

non-fractured porous media, applying the same concept to highly porous materials, where high-aspect-ratio pores are abundant, is not reasonable. As shown in this figure, PTM pore size distributions closely match the trend of the GeoDict pore size distribution curves for low-porosity media. But as the porosity increases, the discrepancy increases.

Another observation in Fig. 5 is the oscillations in the results of both GeoDict and PTM for higher porosity materials, which are mostly due to the wider pore size distribution in these materials. Note that same resolution has been used for all cases. If we decrease the resolution, some of these oscillations will vanish.
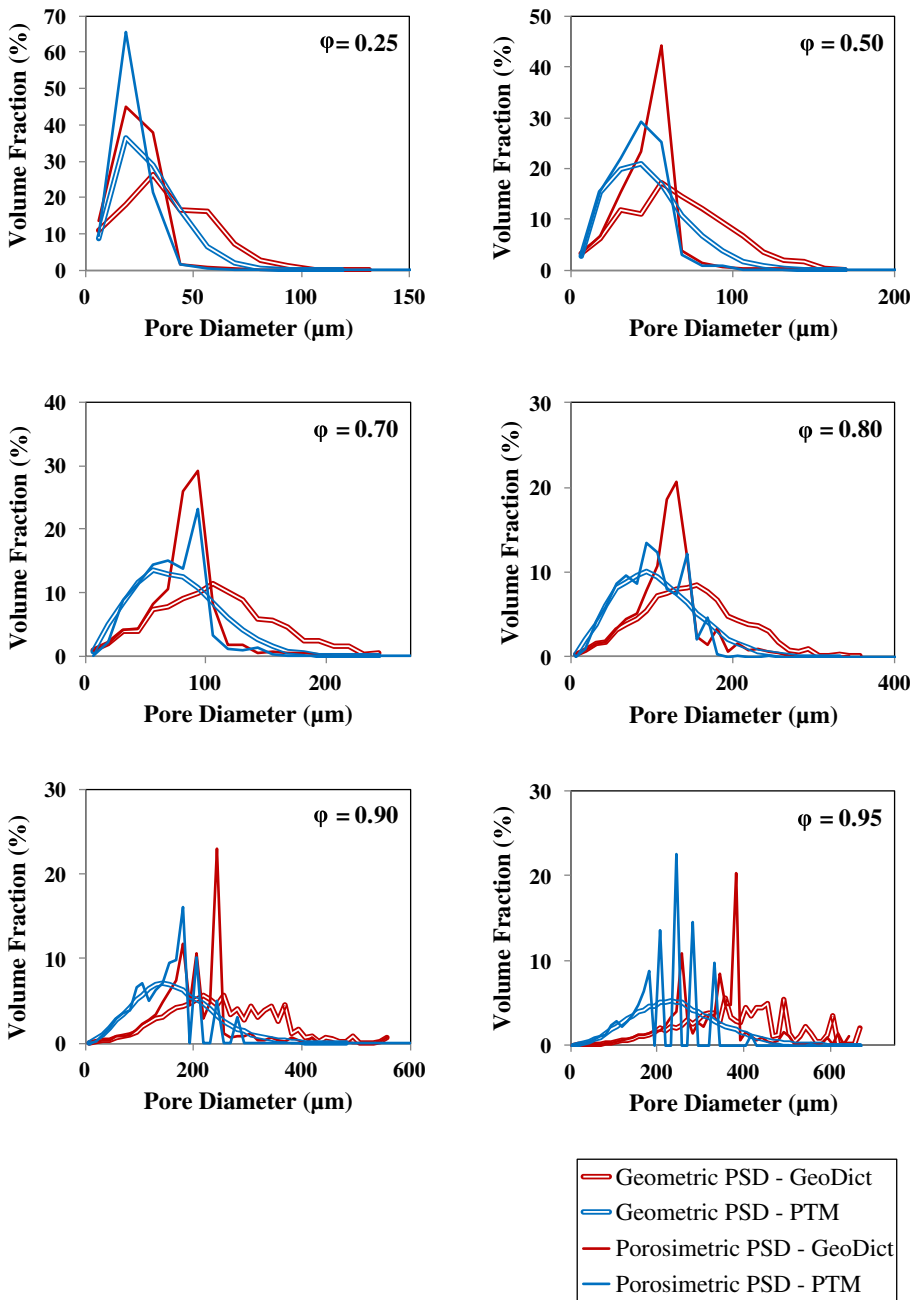
3.2 Absolute Permeability

Figure 6 compares permeability computed in PTM with three other studies on isotropic fibrous materials. These works include that of Nabovati et al. (2009), in which they derived an empirical equation for absolute permeability of isotropic fibrous materials based on their lattice Boltzmann simulation results and works of Tahir and Vahedi Tafreshi (2009) and Palakurthi (2014), who performed finite volume method simulations with FLUENT and OpenFOAM packages, respectively. PTM is in excellent agreement with these numerical results.

3.3 Quasi-Static Drainage and Imbibition

Figure 7 shows the capillary pressure–saturation curves for primary drainage and imbibition for all six fibrous material samples using PTM and FM. The FM simulations have been performed using the GeoDict software package. FM uses morphological operations to determine the flow (or open) paths inside the pore space (Hazlett 1995; Hilpert and Miller 2001). The results are in very good agreement; errors range from 1.14 to 16.51 %. The FM method produces drainage results comparable to the Lattice–Boltzmann method and was chosen for

Fig. 5 Pore size distributions computed with GeoDict and PTM, using porosimetric and geometric methods, for materials ranging in porosity from $\varphi = 0.25$ to $\varphi = 0.95$
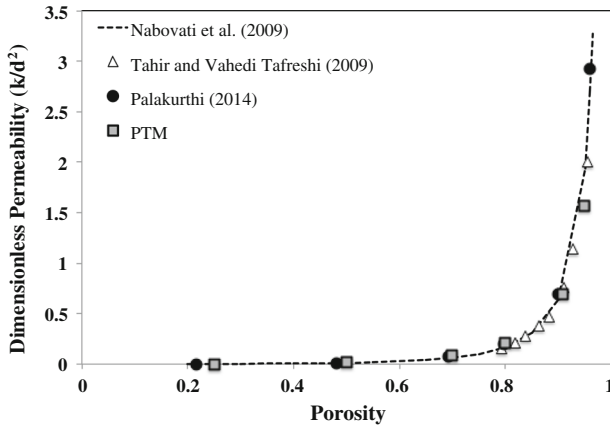
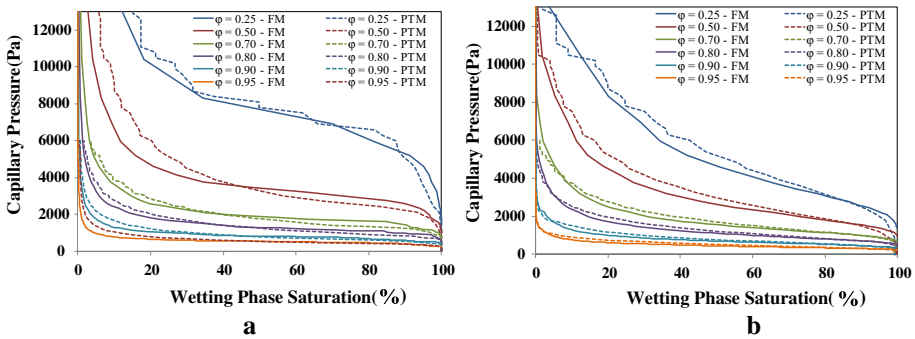**Fig. 6** Absolute transverse permeability versus porosity

Fig. 7 Capillary pressure–saturation curve for **a** primary drainage and **b** primary imbibition in six GeoDict samples

comparison due to its low computational cost and ease of implementation (Vogel et al. 2005). To capture small pores in samples of 25 and 50 % porosity, we increased the resolution from 4 to 2 μm.

The values of capillary pressure versus porosity at 50 % saturation are shown in Fig. 8. This plot clearly shows that PTM results are in excellent agreement with FM, particularly for drainage. Note that full morphology method is known for its accuracy in drainage simulations, but not in imbibition (Vogel et al. 2005). Figure 8 also shows that PTM can capture the geometrical hysteresis that is present in capillary pressure–saturation curves.

Finally, for a material of 80 % porosity, we compared primary drainage curves generated with volume of fluid (VOF) (Palakurthi 2014), FM and PTM (Fig. 9), with excellent agreement.

4 Discussion

This work was inspired by challenges in characterization and flow simulations in thin, highly porous media. Our goal was to develop a fast method for microscale modeling in thin, highly porous materials, but potentially applicable to porous materials with any porosity and void

Fig. 8 Capillary pressure–saturation curve for primary drainage in an 80 % porosity isotropic fibrous GeoDict sample using volume of fluid (VOF), full morphology (FM), and pore topology method (PTM)
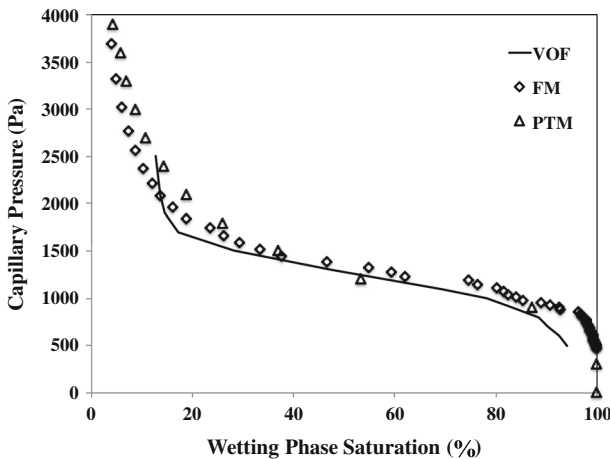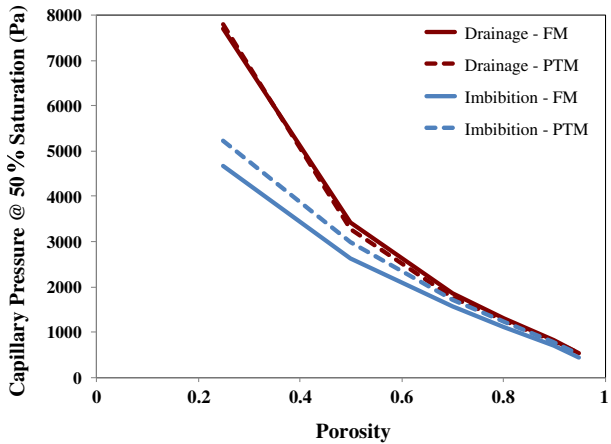
Fig. 9 Capillary pressure–saturation curve for primary drainage using volume of fluid (VOF), full morphology (FM), and pore topology method (PTM)

space geometry. In this study, we probed the suitability of PTM as a possible candidate. Through numerical experiments presented here, we sought to answer two questions: (i) does the medial surface of the void space extracted with PTM's modified MLSEC-ST algorithm possess high reconstructive power and, therefore, serve as a meaningful representative geometry for porous media? If yes, (ii) can this geometry be directly used as the solution domain for multi-phase flow simulations? Our results to date provide positive answers to both inquiries.

One way to assess how well a medial surface represents the structure of the void space is to estimate the statistical properties of the void space based on the information contained in the medial surface. Figure 5 shows the geometric and porosimetric pore size distributions for all six materials, computed with GeoDict and PTM. Overall, both geometric and porosimetric pore size distribution curves derived via PTM follow the same trend and spectrum as those derived using GeoDict software package. The shift toward the lower pore sizes observed in PTM with respect to GeoDict results is due to differences in how pores are defined. In GeoDict, an inscribed sphere in the void space represents a pore. In PTM, on the other hand, a pore is defined as a voxel-wide square prism centered at each voxel on the medial surface and

perpendicular to the medial surface at that voxel. PTM, therefore, would count more pores of smaller sizes. Despite these algorithmic differences, pore size distributions for all tested materials from low to high porosity yielded curves in the same range and of comparable values, lending confidence in the reconstructive power of the medial surfaces used in PTM.

The degree of fidelity of a medial surface to the structure of the void space can be further tested indirectly, through numerical simulations of multi-phase flow. We designed simple numerical experiments to implement percolation and to solve partial differential equations on medial surface. In particular, permeability calculations demonstrate that PTM accurately captures pore connectivity. Our results presented in Figs. 5, 6, 7, 8, and 9 demonstrate a good agreement with state-of-the-art methods and confirm that PTM's medial surfaces (1) have adequate reconstructive power and (2) can be used directly as the solution domain for multi-phase flow simulations.

Numerical experiments presented here were based on several simplifying assumptions and did not utilize all information that can potentially be contained in the medial surface. We searched for the interfaces using the contact angle and the distance to the closest solid wall. This strategy does not include interface stability conditions or trapping assumptions and therefore may result in possible false detection of interfaces and may miss merging and splitting of interfaces. To find the exact location of quasi-static interfaces in capillary dominated flows, detailed geometry of the local cross sections, the 3-D orientation of surrounding solid walls, and the location of other interfaces will be included in the algorithm in the future.

Although the assumption of laminar, fully developed flow between two parallel plates works well for sheet-like, high-aspect-ratio cross sections, it may cause errors when low-aspect-ratio pores are dominant, typically for very low-porosity media. Removing these limitations and relaxing the simplifying assumptions will likely result in higher reconstructive power of the medial surfaces. Again, more geometrical and topological information should be incorporated into the algorithms. Such information is inherent to the medial surface and its attributes such as the distance map. These steps will lead to more realistic assumptions in PTM formulation and help extend its applicability to a wider range of porous media, including non-fibrous materials

5 Conclusions

In this article, we introduced the pore topology method (PTM), a fast, microscale modeling approach based on representing the void space of porous medium by its medial surface and using it as the solution domain for multi-phase flow computations. To validate PTM, we simulated quasi-static drainage and imbibition and computed pore size distributions and absolute permeability for a set of isotropic fibrous materials of varying porosity. Our results are in very good agreement with several state-of-the-art methods such as lattice Boltzmann, full morphology, volume of fluid, and finite volume methods, as well as analytical solutions. Future work will focus on increasing the reconstructive power of the medial surface through incorporating more detailed spatial information about the porous media structure into the medial surface.

Appendix 1: Medial Surface Extraction Algorithm

In this appendix, we demonstrate the medial surface extraction algorithm on a simple, constant cross-sectional prism shown in Fig. 10. The algorithm outlined here is based on the formulation provided in Vera et al. (2012a). As mentioned earlier, we have modified the last step of the algorithm, medial surface thinning, to ensure full connectivity in the final medial surface.

Step 1: Obtain a Binary Image of Porous Media

Since the medial surface extraction algorithm described here is a voxel-based approach, obtaining a voxelized binary image of porous media is essential. Binary images for porous materials can be obtained either by using 3-D imaging of actual materials, or by using commercial packages like GeoDict. In the binary image shown in Fig. 10, we labeled voxels of the solid matrix as one, and of void space as zero.

Step 2: Generate Euclidean Distance Map (D)

From the binary image of the porous medium, we generate the distance map inside the void space. Distance map D, also known as distance field or distance transform, is a representation of a digital image based on the distance between each voxel and the closest boundary (solid phase). Assuming solid voxels (1-value voxels) as boundary voxel, the distance map of the void space can be generated by computing the distance between each void voxel and the closest solid voxel. Figure 11 shows the distance map of the sample prism.

Step 3: Compute Gradient of Distance Map

The gradient of distance map can be computed by convolving the distance map with gradients of Gaussian kernel:

$$\nabla D = \left(\partial_x D_\sigma, \partial_y D_\sigma, \partial_z D_\sigma \right) = \left(\partial_x g_\sigma * D, \partial_y g_\sigma * D, \partial_z g_\sigma * D \right) \tag{8}$$
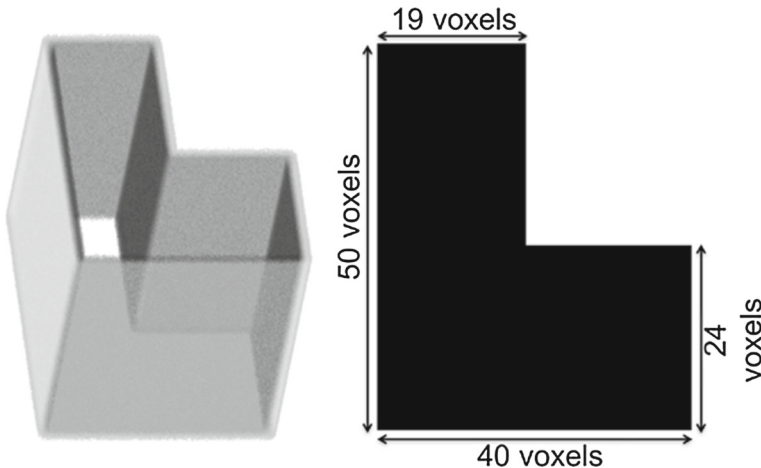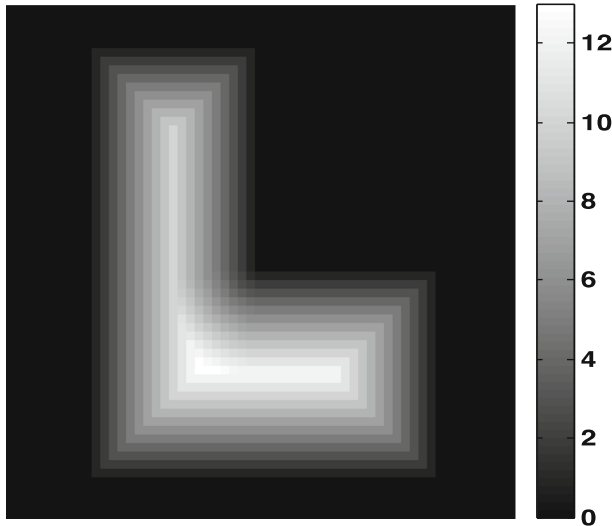

Fig. 10 3-D model of the prism used in this example and its 2-D binary representation

Fig. 11 2-D slice of the distance map generated in the prism of Fig. 10

where $\partial_x g_\sigma$, $\partial_y g_\sigma$, and $\partial_z g_\sigma$ are partial derivatives of the Gaussian kernel g with standard deviation of σ and $*$ is the convolution operator. To avoid over-smoothing, we used $3 \times 3 \times 3$ voxels window kernels with $\sigma = 0.5$.

Step 4: Compute Structure Tensor (ST)

The structure tensor (ST) summarizes the dominant directions of the gradients in a neighborhood of each voxel and is derived from the gradient field of a function. Smoothed ST at each voxel can be computed as

$$ST_{\rho,\sigma}(D) = \begin{pmatrix} g_\rho * \partial_x D_\sigma{}^2 & g_\rho * \partial_x D_\sigma \partial_y D_\sigma & g_\rho * \partial_x D_\sigma \partial_z D_\sigma \\ g_\rho * \partial_y D_\sigma \partial_x D_\sigma & g_\rho * \partial_y D_\sigma{}^2 & g_\rho * \partial_y D_\sigma \partial_z D_\sigma \\ g_\rho * \partial_z D_\sigma \partial_x D_\sigma & g_\rho * \partial_z D_\sigma \partial_y D_\sigma & g_\rho * \partial_z D_\sigma{}^2 \end{pmatrix} \qquad (9)$$

where g_ρ is a $3 \times 3 \times 3$ Gaussian kernel with standard deviation of ρ. Here we chose $\rho = 1$.

Step 5: Find Principal Eigenvectors

ST is a positive definite tensor; therefore, it has three nonnegative eigenvalues for a 3-D problem. For this case, since we have built the structure tensor from the gradients of the distance map, the eigenvectors at each voxel are the directions of principal gradients of distance map at the neighborhood of that voxel. To find the direction of the maximum gradient at each voxel, one needs to find the principal eigenvector of ST (i.e., the eigenvector corresponding to the eigenvalue of largest magnitude) at that voxel. For the sample prism of Fig. 10, the 2-D view of the principal eigenvector field (**V**) is shown in Fig. 12.

Step 6: Reorient Principal Eigenvectors in the Direction of Gradient

To prepare the vector field for step 7, we need all the principal eigenvectors to point toward the downward gradient. Reorienting the principal eigenvectors toward the downward gradient can
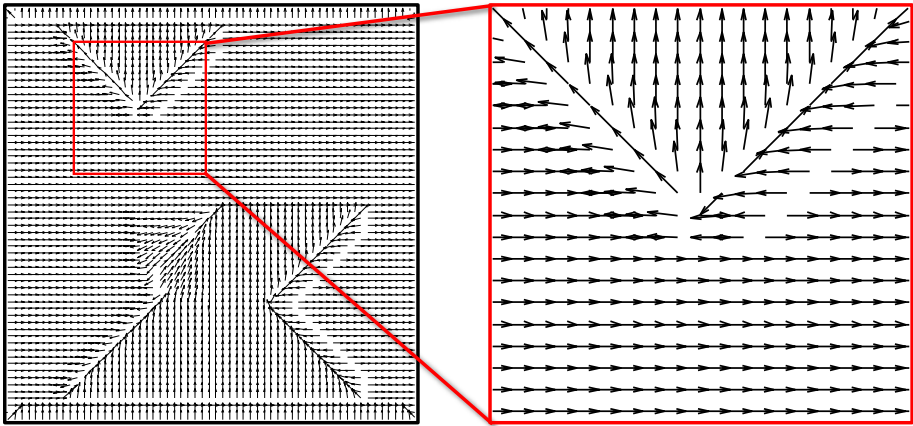
Fig. 12 2-D view of the principal eigenvector field (**V**) of the prism
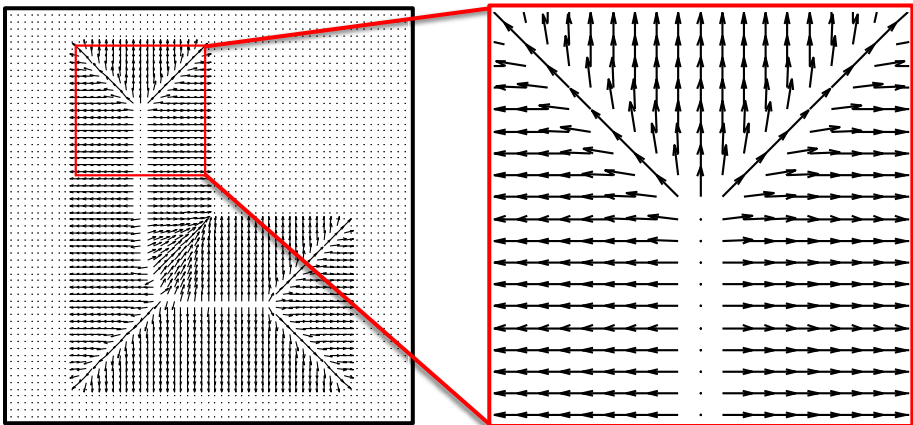

**Fig. 13** 2-D view of the reoriented principal eigenvector field (**V**) of the prism

be done by multiplying each vector by the sign of the scalar product of principal eigenvector and the gradient at each voxel:

$$V = \text{sign}\,(V \cdot \nabla D) \cdot V \qquad (10)$$

As shown in Fig. 13, besides reorienting the principal eigenvector field, this assigns zero to zero-gradient voxels.

Step 7: Compute Normalized Ridge Map (NRM)

Since the magnitude of all vectors in V is less than or equal to one, taking the divergence of V will assign a value between N and $+N$ to each voxel, where N is the dimension of the problem. For a 3-D geometry, this value will be bounded between -3 and $+3$. We will refer to this value as the normalized ridge map (NRM). Positive NRMs correspond to ridge voxels and negative to valley voxels; therefore, the magnitude of NRM value represents the degree of ridgeness or valleyness. NRM can be calculated as
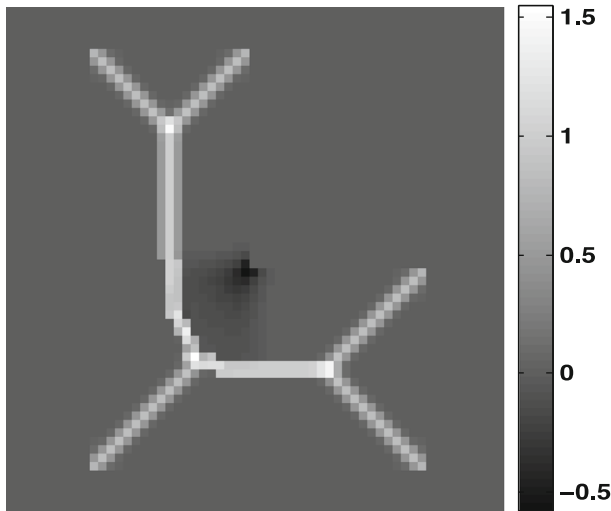
Fig. 14 2-D slice of the normalized ridge map generated for the sample prism

$$\text{NRM} = \text{div}\,(V) \tag{11}$$

A 2-D view of NRM for the sample prism is shown in Fig. 14. For the purpose of medial surface extraction, we are only interested in ridges (positive NRMs); therefore, non-positive values can be ignored at the end of this step.

### Step 8: Medial Surface Thinning: Hessian-Based Non-maxima Suppression

The last step is to apply a thinning algorithm on the positive NRM values to extract a voxel-wide medial surface. One of the most common thinning algorithms is non-maxima suppression (NMS). In NMS, one first needs to find a suppression direction, which is the direction perpendicular to the medial surface. The common practice is to use the direction of principal gradient of the NRM at each voxel as the suppression direction. It should be noted that the direction of principal gradient of NRM is the principal eigenvector of the structure tensor of NRM. However, it has been shown that implementing NMS on NRM map will introduce holes (disconnectivities) in the medial surface (Vera et al. 2012a). Although this drawback can be ignored in many image processing cases, for our application it will change the connectivity of the void space of the porous media, which is undesirable. To overcome this drawback, we propose a modified NMS algorithm based on using the direction of maximum curvature of NRM as the suppression direction. The direction of maximum curvature of NRM is the principal eigenvector of Hessian tensor of NRM. Hessian matrix is a symmetric matrix that summarizes the dominant directions of curvatures at a neighborhood of a voxel. Instead of using the structure tensor of NRM, modified NMS uses the Hessian tensor of NRM map to find the suppression direction. Throughout this paper, we will refer to this non-maxima suppression method as the Hessian-based non-maxima suppression (HNMS).

In HNMS, the principal eigenvector of Hessian tensor of NRM at each point is chosen as the suppression direction. We computed the Hessian matrix at each voxel as below:

$$H_{\rho,\sigma}\,(\text{NRM}) = \begin{pmatrix} \partial_{xx}g_\rho * \text{NRM} & \partial_{xy}g_\rho * \text{NRM} & \partial_{xz}g_\rho * \text{NRM} \\ \partial_{yx}g_\rho * \text{NRM} & \partial_{yy}g_\rho * \text{NRM} & \partial_{yz}g_\rho * \text{NRM} \\ \partial_{zx}g_\rho * \text{NRM} & \partial_{zy}g_\rho * \text{NRM} & \partial_{zz}g_\rho * \text{NRM} \end{pmatrix} \tag{12}$$
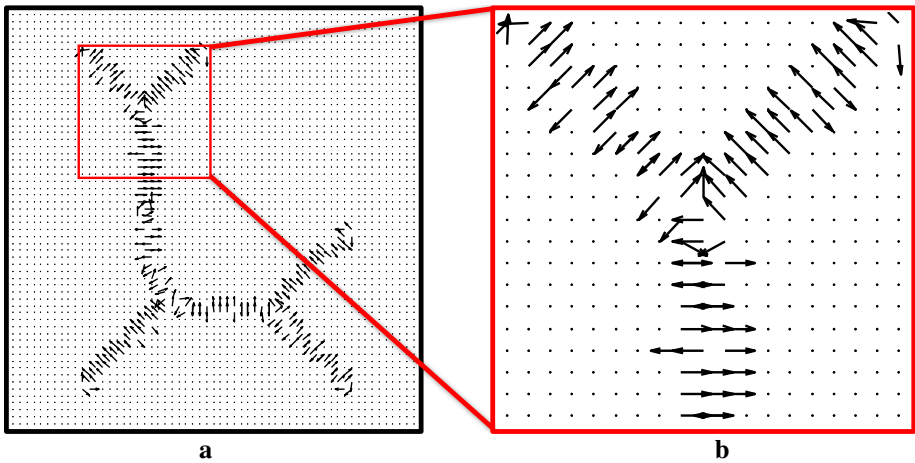
Fig. 15 **a** Suppression directions for Hessian-based NMS (V_{HNMS}) and **b** enlarged view of the area *marked* by the *red square* in Fig. 15a
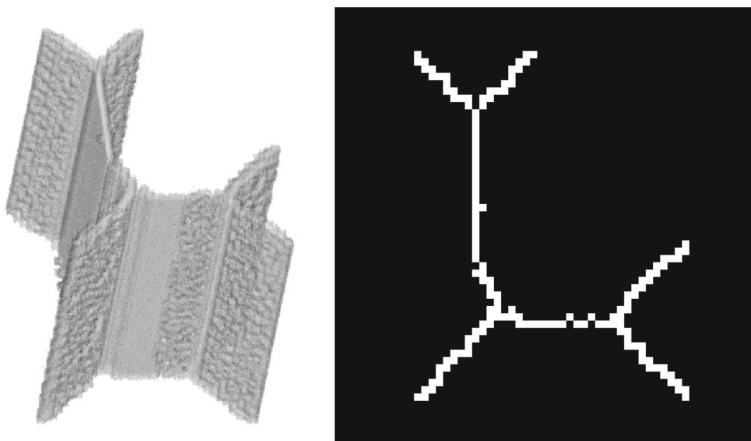
Fig. 16 Extracted medial surface for the prism in Fig. 10

where $\partial_{x_i x_j} g_\rho$ is the second derivative of the Gaussian kernel with respect to coordinates x_i and x_j, and $\rho = 1$. Let V_{HNMS} be the principal eigenvector of the Hessian matrix at each voxel. The non-maxima suppression can be computed as

$$
\text{NMS}\,(x, y, z) = \begin{cases} 1 & \text{if NRM}\,(x, y, z) > \max\left\{\text{NRM}\left(V^+_{\text{HNMS}}\right), \text{NRM}\left(V^-_{\text{HNMS}}\right)\right\} \\ 0 & \text{otherwise} \end{cases} \tag{13}
$$

where $\text{NRM}\left(V^+_{\text{HNMS}}\right)$ and $\text{NRM}\left(V^-_{\text{HNMS}}\right)$ are NRM values in the immediate neighborhood of a voxel in the direction of V_{HNMS}.

Figure 15 shows the suppression directions in the proposed Hessian-based NMS. It should be noted that the ideal suppression direction should be perpendicular to the medial surface. Finally, Fig. 16 shows 2-D and 3-D views of the extracted medial surface for the sample prism.

Appendix 2: Hydraulic Conductivity of Prisms

To test the validity of the planar flow assumption in computing local conductivities in Eq. (2), we computed hydraulic conductivities for a set of prisms with polygonal cross sections using the PTM permeability calculation algorithm and compared the result with exact solutions derived by Mortensen et al. (2005). We followed the procedure outlined in Sect. 2.2, but instead of Eq. (4), we used the following expression for the hydraulic conductivity K of the prism:

$$K = -\frac{QL}{\Delta P} \tag{14}$$

As in Mortensen et al. (2005), we defined the dimensionless hydraulic resistivity or correction factor α, and dimensionless compactness C, to represent our results. These parameters can be computed as follows:

$$\alpha = \frac{A^2}{K\mu} \tag{15}$$

$$C = \frac{p}{A^2} \tag{16}$$

where A and p are the cross-sectional area and cross-sectional perimeter of the prism, respectively; K is hydraulic conductivity; and μ is fluid viscosity. Figure 17 compares the PTM results with exact values for α and C computed in Mortensen et al. (2005), for rectangular and triangular prisms. As the compactness increases, the PTM results approaches the exact solution, which is consistent with our assumption of flow between parallel plates for all voxels on medial surface.

Appendix 3: Discretization of Eq. (1)

As mentioned in Sect. 2.2, to find the pressure field inside the void space, the following equation is discretized and solved on the medial surface of the void space:

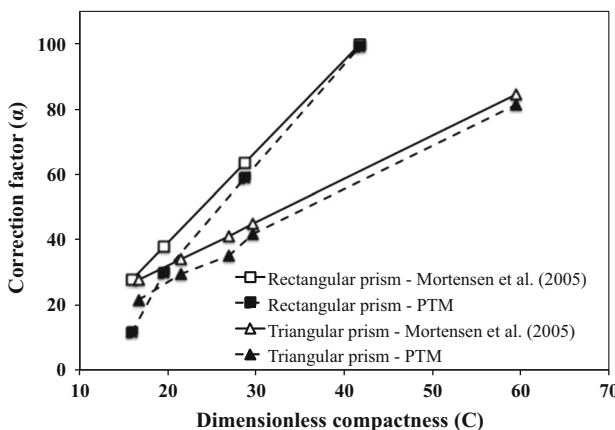$$\nabla \cdot (K_{\text{local}} \nabla P) = 0 \tag{17}$$

Fig. 17 Correction factor versus dimensionless compactness for triangular and rectangular prisms

where K_{local} is the local hydraulic conductivity at each voxel of the medial surface, and its value is zero on all non-medial surface voxels in the porous media domain.

Since we are aiming to discretize and solve this equation only on the medial surface, we have used a modified version of the well-known central differencing scheme used in finite volume method (FVM).

Following the finite volume approach, we start the discretization by taking the integral of both sides of Eq. (17) over the volume of a voxel (V).

$$\int_V \nabla \cdot (K_{local}\nabla P)\, dV = 0 \tag{18}$$

Then, using the divergence theorem, we can change the above volume integral to a surface integral:

$$\int_S (K_{local}\nabla P) \cdot \boldsymbol{n}\,dS = 0 \tag{19}$$

So far, we have been followed the exact procedure that one would take in FVM. Then, instead of using the six faces of our cubic voxels as our integration surfaces, we assumed an imaginary rhombicuboctahedron with 26 equal-area faces. Using this analogy, instead of three gradient directions, we will have 13 directions:

$$\sum_{i=1}^{13}\left[\left[K_{local}\frac{\partial P}{\partial \boldsymbol{n_i}}\right]_{i^+} - \left[K_{local}\frac{\partial P}{\partial \boldsymbol{n_i}}\right]_{i^-}\right] = 0 \tag{20}$$

where $\boldsymbol{n_i}$ is the gradient direction and i^+ and i^- shows the opposite faces along the gradient direction. This assumption is essential in capturing all curvatures and the junctions that are present in the voxel-wide medial surface.

Further simplification of Eq. (20) will result:

$$\sum_{i=1}^{13}\left[\left[\left(K_{local,i+1} + K_{local,i}\right)\left(P_{i+1} - P_i\right)\right]\text{sign}(K_{local,i+1})\right.$$
$$\left. - \left[\left(K_{local,i} + K_{local,i-1}\right)\left(P_i - P_{i-1}\right)\right]\text{sign}(K_{local,i-1})\right] = 0 \tag{21}$$

In Eq. (21), sign($\cdot$) is used to automatically zero out the gradient between a medial surface voxel and a non-medial surface voxel.

References

Ahrenholz, B., Tölke, J., Lehmann, P., Peters, A., Kaestner, A., Krafczyk, M., Durner, W.: Prediction of capillary hysteresis in a porous material using lattice-Boltzmann methods and comparison to experimental data and a morphological pore network model. Adv. Water Resour. **31**, 1151–1173 (2008)

Bazylak, A., Berejnov, V., Markicevic, B., Sinton, D., Djilali, N.: Numerical and microfluidic pore networks: towards designs for directed water transport in GDLs. Electrochim. Acta **53**, 7630–7637 (2008)

Blum, H.: A transformation for extracting new descriptors of shape. Models Percept. Speech Vis. Form **19**, 362–380 (1967)

Bouix, S., Siddiqi, K., Tannenbaum, A.: Flux driven automatic centerline extraction. Med. Image Anal. **9**, 209–221 (2005)

Corbett, P., Hayashi, F., Alves, M., Jiang, Z., Wang, H., Demyanov, V., Machado, A., Borghi, L., Srivastava, N.: Microbial carbonates: a sampling and measurement challenge for petrophysics addressed by capturing the bioarchitectural components. Geol. Soc. Lond. Spec. Publ. **418**, 69–85 (2015)

Frette, O.I., Helland, J.O.: A semi-analytical model for computation of capillary entry pressures and fluid configurations in uniformly-wet pore spaces from 2D rock images. Adv. Water Resour. **33**, 846–866 (2010)

Gervais, P.-C., Bardin-Monnier, N., Thomas, D.: Permeability modeling of fibrous media with bimodal fiber size distribution. Chem. Eng. Sci. **73**, 239–248 (2012)

Ghassemzadeh, J., Hashemi, M., Sartor, L., Corp, A.D., Dennison, A.: Pore network simulation of imbibition into paper during coating: I. Model development. AIChE J. **47**, 519–535 (2001)

Ghassemzadeh, J., Sahimi, M.: Pore network simulation of fluid imbibition into paper during coating: II. Characterization of paper's morphology and computation of its effective permeability tensor. Chem. Eng. Sci. **59**, 2265–2280 (2004)

Gostick, J.T.: Random pore network modeling of fibrous PEMFC gas diffusion media using Voronoi and Delaunay tessellations. J. Electrochem. Soc. **160**, F731–F743 (2013)

Gostick, J.T., Ioannidis, M.A., Fowler, M.W., Pritzker, M.D.: Pore network modeling of fibrous gas diffusion layers for polymer electrolyte membrane fuel cells. J. Power Sources **173**, 277–290 (2007)

Hazlett, R.: Simulation of capillary-dominated displacements in microtomographic images of reservoir rocks. Transp. Porous Media **20**, 21–35 (1995)

Hilpert, M., Miller, C.: Pore-morphology-based simulation of drainage in totally wetting porous media. Adv. Water Resour. **24**, 243–255 (2001)

Hinebaugh, J., Bazylak, A.: Condensation in PEM fuel cell gas diffusion layers: a pore network modeling approach. J. Electrochem. Soc. **157**, B1382–B1390 (2010)

Jiang, Z., van Dijke, R., Geiger, S., Couples, G., Wood, R.: Extraction of fractures from 3D rock images and network modelling of multi-phase flow in fracture-pore systems. In: International Symposium of the Society of Core Analysts, Aberdeen, Scotland (2012)

Jiang, Z., Wu, K., Couples, G., van Dijke, M.I.J., Sorbie, K.S., Ma, J.: Efficient extraction of networks from three-dimensional porous media. Water Resour. Res. **43**, 1–17 (2007)

Joekar-Niasar, V., Prodanović, M., Wildenschild, D., Hassanizadeh, S.M.: Network model investigation of interfacial area, capillary pressure and saturation relationships in granular porous media. Water Resour. Res. **46**, W06526 (2010)

Koido, T., Furusawa, T., Moriyama, K.: An approach to modeling two-phase transport in the gas diffusion layer of a proton exchange membrane fuel cell. J. Power Sources **175**, 127–136 (2008)

Lee, K., Nam, J., Kim, C.: Pore-network analysis of two-phase water transport in gas diffusion layers of polymer electrolyte membrane fuel cells. Electrochim. Acta **54**, 1166–1176 (2009)

Lee, K., Nam, J., Kim, C.: Steady saturation distribution in hydrophobic gas-diffusion layers of polymer electrolyte membrane fuel cells: a pore-network study. J. Power Sources **195**, 130–141 (2010)

Lee, T., Kashyap, R., Chu, C.: Building skeleton models via 3-D medial surface axis thinning algorithms. CVGIP Graph. Models Image Process. **56**, 462–478 (1994)

Lindquist, W.: The geometry of primary drainage. J. Colloid Interface Sci. **296**, 655–668 (2006)

Lindquist, W., Venkatarangan, A.: Investigating 3D geometry of porous media from high resolution images. Phys. Chem. Earth A Solid Earth Geod. **24**, 593–599 (1999)

Lopez, A., Lloret, D., Serrat, J., Villanueva, J.: Multilocal creaseness based on the level-set extrinsic curvature. Comput. Vis. Image Underst. **77**, 111–144 (2000)

Markicevic, B., Bazylak, A., Djilali, N.: Determination of transport parameters for multiphase flow in porous gas diffusion electrodes using a capillary network model. J. Power Sources **171**, 706–717 (2007)

Mason, G., Morrow, N.R.: Capillary behavior of a perfectly wetting liquid in irregular triangular tubes. J. Colloid Interface Sci. **141**, 262–274 (1991)

Mortensen, N., Okkels, F., Bruus, H.: Reexamination of Hagen-Poiseuille flow: shape dependence of the hydraulic resistance in microchannels. Phys. Rev. E **71**, 057301 (2005)

Nabovati, A., Llewellin, E., Sousa, A.: A general model for the permeability of fibrous porous media based on fluid flow simulations using the lattice Boltzmann method. Compos. A **40**, 860–869 (2009)

Palakurthi, N.: Direct Numerical Simulation of Liquid Transport Through Fibrous Porous Media. Ph.D. dissertation, University of Cincinnati (2014)

Pan, S., Davis, H., Scriven, L.: Modeling moisture distribution and binder migration in drying paper coatings. Tappi J. **78**, 127–143 (1995)

Prat, M., Agaësse, T.: Thin porous media. In: Vafai, K. (ed.) Handbook of Porous Media (Chapter 4), 3rd edn.Taylor & Francis, London (2015)

Price, M.A., Armstrong, C.G., Sabin, M.A.: Hexahedral mesh generation by medial surface subdivision: Part I. Solids with convex edges. Int. J. Numer. Methods Eng. **38**, 3335–3359 (1995)

Prodanovic, M., Bryant, S.: Physics-driven interface modeling for drainage and imbibition in fractures. SPE J. **14**, 532–542 (2009)

Prodanović, M., Bryant, S.: A level set method for determining critical curvatures for drainage and imbibition. J. Colloid Interface Sci. **304**, 442–458 (2006)

Pudney, C.: Distance-ordered homotopic thinning: a skeletonization algorithm for 3D digital images. Comput. Vis. Image Underst. **72**, 404–413 (1998)

Qin, C., Hassanizadeh, S.: Multiphase flow through multilayers of thin porous media: General balance equations and constitutive relationships for a solid–gas–liquid three-phase system. Int. J. Heat Mass Transf. **70**, 693–708 (2014)

Riasi, M.S., Huang, G., Montemagno, C., Yeghiazarian, L.: A General 3-D Methodology for Quasi-Static Simulation of Drainage and Imbibition: Application to Highly Porous Fibrous Materials. AGU Fall Meeting Abstracts, San Francisco (2013)

Schulz, V.P., Wargo, E.A., Kumbur, E.C.: Pore-morphology-based simulation of drainage in porous media featuring a locally variable contact angle. Transp. Porous Media **107**, 13–25 (2015)

Si, C., Wang, X., Yan, W., Wang, T.: A comprehensive review on measurement and correlation development of capillary pressure for two-phase modeling of proton exchange membrane fuel cells. J. Chem. **2015**, 1–17 (2015)

Styner, M., Lieberman, J., Pantazis, D., Gerig, G.: Boundary and medial shape analysis of the hippocampus in schizophrenia. Med. Image Anal. **8**, 197–203 (2004)

Sun, H., Frangi, A., Wang, H.: Automatic cardiac MRI segmentation using a biventricular deformable medial model. Med. Image Comput. Comput. Assist. Interv. MICCAI **2010**, 468–475 (2010)

Tahir, M.A., Vahedi Tafreshi, H.: Influence of fiber orientation on the transverse permeability of fibrous media. Phys. Fluids **21**, 083604 (2009)

Vennat, E., Attal, J.-P., Aubry, D., Degrange, M.: Three-dimensional pore-scale modelling of dentinal infiltration. Comput. Methods Biomech. Biomed. Eng. **17**, 632–642 (2014)

Vera, S., Gil, D., Borras, A., Sánchez, X., Párez, F., Linguraru, M., González Ballester, M.A.: Computation and evaluation of medial surfaces for shape representation of abdominal organs. In: Yoshida, H. et al. (eds.) Abdominal Imaging 2011, LNCS 7029, pp. 223–230 (2012a)

Vera, S., González, M., Gif, D.: A medial map capturing the essential geometry of organs. In: 2012 International Symposium on Biomedical Imaging (2012b)

Vogel, H.J., Tölke, J., Schulz, V.P., Krafczyk, M., Roth, K.: Comparison of a lattice-Boltzmann model, a full-morphology model, and a pore network model for determining capillary pressure–saturation relationships. Vadose Zone J. **4**, 380–388 (2005)

Wildenschild, D., Sheppard, A.: X-ray imaging and analysis techniques for quantifying pore-scale structure and processes in subsurface porous medium systems. Adv. Water Resour. **51**, 217–246 (2013)

Wu, R., Liao, Q., Zhu, X., Wang, H.: Pore network modeling of cathode catalyst layer of proton exchange membrane fuel cell. Int. J. Hydrog. Energy **37**, 11255–11267 (2012)